



Highly active CoMoS phase on titania nanotubes as new hydrodesulfurization catalysts

J.A. Toledo-Antonio*, M.A. Cortés-Jácome, C. Angeles-Chávez, J. Escobar, M.C. Barrera, E. López-Salinas

Molecular Engineering Program, Instituto Mexicano del Petróleo, Eje Central Lázaro Cárdenas # 152, San Bartolo Atepehuacan, G. A. Madero, 07730 México, D.F., Mexico

ARTICLE INFO

Article history:

Received 1 September 2008

Received in revised form 4 March 2009

Accepted 9 March 2009

Available online 27 March 2009

Keywords:

HDS catalysts

CoMoS phase

Titania nanotubes

X-ray photoelectronic spectroscopy

Raman Spectroscopy

High resolution electron microscopy

ABSTRACT

A series of CoMoS on nanotubular TiO₂ (NT) catalysts were prepared by incipient impregnation at Mo = 3–5 atoms/nm² and Co/(Co + Mo) = 0.2–0.4. A nanotubular TiO₂ (NT) of 5.5 nm inner diameter, 236 m²/g surface area and 0.5 cm³/g total pore volume was prepared and used as support. The CoMoS/NT catalysts were characterized mainly by Raman and XPS spectroscopies, HRTEM and HAADF (high angle annular dark field) detector. The sulfided catalysts were tested in the hydrodesulphurization (HDS) of dibenzothiophene at 320 °C and 56 kg/cm². Inorganic fullerene-like MoS₂ and/or CoMoS particles, made up of 2–6 structural layers, depending on the Co/(Co + Mo) ratio, were observed, smeared along the nanotubes. An estimation of CoMoS phase surface density (δ), after taken into account all sulfided species quantified by XPS spectra, indicated that highest HDS activity (43×10^{-4} m³/kg_{Mo} s) is attained when Mo = 5 atoms/nm² and Co/(Co + Mo) = 0.3. In comparison, at a lower (0.2) or higher (0.4) Co/(Co + Mo) ratio, either segregated MoO₃ or Co₉S₈ phases were detected, respectively, with Co sulfidability decreasing 60–42%, respectively, and HDS activity being considerably lower.

© 2009 Elsevier B.V. All rights reserved.

1. Introduction

The more stringent environmental regulations concerning maximum sulfur content in liquid fuels, e.g., <15 ppm, have been the driving force for oil refineries to produce ultra-low sulfur fuels at affordable cost, upgrading existing technologies and developing new processes and more active hydrodesulfurization (HDS) catalysts. The application of the later could enhance the productivity and improve the product quality without negative impact on capital investment.

Industrially, HDS reaction is carried out on CoMoS/Al₂O₃ or NiMoS/Al₂O₃ catalysts. The properties of the sulfided catalyst strongly depend on the interaction with the support and on the promotion degree of MoS₂ by the adjacent Co and Ni sulfides yielding the so called “CoMoS” or “NiMoS” phases, [1,2] which are considered to contain the active sites for HDS reactions. It has been reported that coordinatively unsaturated sites occur at edges and corners of MoS₂ crystallites. For alumina-supported catalysts the sites have been classified as type 1, when present on monolayer MoS₂ slabs, and type 2, when in highly stacked MoS₂ particles [3]. CoMoS type 2 sites are about twice as active as type 1 [4]. Then, the

formation of highly dispersed CoMoS type 2 sites may result in highly active CoMo sulfided catalysts. However, CoMoS phase formation is not an easy task, and strongly depends on the interaction degree between Mo oxide (e.g., precursor to MoS₂) and the support. In alumina-supported catalysts for example, the surface is often modified with additives such as phosphorous, fluorine or boron [5,6] to adequately obtain improved Mo oxides dispersion, and in order to control morphology, size and stacking number of MoS₂ particles.

Other strategies applied to generate highly active CoMoS type 2 sites involve replacing the conventional alumina support by other metal oxides showing less interaction with deposited Mo oxides such as SiO₂ [7], TiO₂ [8,9], ZrO₂ [10] or mixed oxides [11,12]. Thus, great interest is being devoted to study the effect of the support on the HDS catalytic activity of CoMoS and NiMoS sulfided catalysts. One of the most interesting supports for HDS catalysts is titania, since a considerable increase in intrinsic HDS activity has been reported for MoS₂ when supported on anatase TiO₂, in comparison with a similar composition on an alumina carrier [8,13]. However, the TiO₂ low specific surface area (SSA) (e.g., <60 m²/g) limits its industrial application as HDS catalyst support. Recently, TiO₂ with relatively high SSA (140–175 m²/g) have been developed, with good enough textural properties to efficiently disperse CoMoS phase [14,15]. These improved formulations may have a beneficial impact on the production of ultra-low sulfur diesel (ULSD).

* Corresponding author.

E-mail address: jtoledo@imp.mx (J.A. Toledo-Antonio).

In the last decade, anatase TiO₂ has been converted into titania nanotubes or nanofibers through a relatively simple alkaline hydrothermal method [16–19], representing a suitable route for rapid manufacturing scale-up. The nanotubes exhibit large internal and external surfaces, along with surface in the vertex and in the interlayer regions that compose the nanotube walls [20,21]. In fact, the transformation of titania into nanotubes yields materials with SSA as large as 400 m²/g [17,22], with high pore volume and inner diameters around 7 nm, opening possibilities to disperse a larger amount of transition metal oxides or sulfides. In a recent work, we have shown that titania nanotubes can disperse efficiently 20 wt.% of WO₃ maintaining the nanotubular morphology and SSA being as high as 210 m²/g after annealing at 400 °C [23].

Present and future trends in commercial catalysts developments for ULSD production, point out towards the increase of active phase loading from 3 Mo atoms/nm², for conventional catalysts, to around 5–8 atoms/nm² [24]. Recently, we have optimized the impregnation procedure by adjusting the pH of the Co and Mo solutions at 5.6, for samples with Mo loading of 3 atoms/nm² [25]. In this work, the effect of metal loading on nanotubular titania support was studied by increasing Mo content from 3 to 5 atoms/nm². As well, the (Co/Co + Mo) atomic ratio was optimized in samples of higher metal loading that showed high HDS activity. The influence of the nanotubular morphology of the support on the CoMoS particles was thoroughly examined by HRTEM.

2. Experimental

2.1. Synthesis of nanotubular titania

Nanotubular titania, used as support, was synthesized by a hydrothermal method, starting from a TiO₂ anatase (Hombitec K03, provided by Sachtleben Chemie). TiO₂ anatase powder was suspended in an aqueous 10 M NaOH solution and the resulting suspension was placed in an autoclave. The hydrothermal reaction was carried out at 100 °C, for 24 h under autogenous pressure and stirring. Thereafter, the white slurry was filtered and neutralized with a 1 M solution of nitric acid (HNO₃) overnight. Then, the material was washed with deionized water and dried at 110 °C yielding a hydrous titania powder with nanotubular morphology.

2.2. Catalysts preparation

CoMo-based catalysts were prepared by incipient wetness impregnation in two steps. In the first step, nanotubular titania (NT) was put in contact with an aqueous ammonium heptamolybdate (AHM) solution at pH 5.6 in order to have 3, 4 and 5 Mo atoms/nm², as indicated in Table 1. In the second step and after drying at 110 °C, Co (through a cobalt acetate aqueous solution) was impregnated on the Mo-containing samples. After impregnation, further processing included drying at 120 °C and annealing at 380 °C under air flow. Samples were labeled as NT-*x*-*y*, where NT stands for nanotubular titania support, “*x*” being the nominal amount of Mo atoms/nm² and “*y*” being the Co/(Co + Mo) atomic ratio. Catalysts sulfidation was carried out on oxidized samples at

380 °C, under a 10 vol.% H₂S/H₂ flow for 2 h. This step was carried out in a Pyrex glass tubular down-flow reactor, the H₂S/H₂ mixture being fed at a ~24 L/h constant flow rate. This routine could be considered as standard in activating HDS catalysts [9,12].

2.3. HDS catalytic test

Sulfided catalysts (~0.2 g) were tested in HDS of dibenzothiophene (DBT, ~0.3 g), model molecule representing S-bearing compounds in middle distillates, in a SS316 batch reactor using *n*-hexadecane (100 ml) as solvent (initial DBT concentration 16.3 μmol/L, 674 ppm S). The reaction temperature was fixed at 320 °C and stirring rate of 1000 rpm. After operating temperature was attained, pure H₂ (UHP) was fed to the reactor to attain 56 kg/cm² (total pressure). Samples of liquid product were analyzed in a Varian 3400 CX gas chromatograph, equipped with a flame ionization detector and a dimethylpolysiloxane (50 m × 0.2 mm × 0.5 μm) capillary column. HDS kinetic constants were calculated assuming pseudo-first order kinetics referred to DBT concentration (*x* = conversion, *t* = time), taking into account that hydrogen was fed in such excess that its partial pressure could be considered constant:

$$k = \frac{-\ln(1-x)}{t} \quad (1)$$

k values for various catalysts were normalized by considering reaction volume and mass of catalyst used (*k* in m³/(kg_{cat} s)). Even though a Langmuir–Hinshelwood protocol could provide important information about reaction kinetics, and that comparing HDS catalysts performance through a pseudo-first order kinetic model could be considered an oversimplification, the later has been recognized as a reliable method in discriminating among various HDS catalytic formulations [12,15].

2.4. Catalysts characterization

Chemical composition of the impregnated materials after annealing at 380 °C was determined by atomic absorption spectroscopy (AAS) in a PerkinElmer 2380 apparatus.

Textural properties were measured in an ASAP-2000 analyzer from Micromeritics. SSA was calculated from N₂ physisorption at –196 °C using the Brunauer–Emmet–Teller (BET) equation. Average pore size was obtained by the Barrett–Joyner–Halenda (BJH) method in the desorption stage. Materials calcined *ex situ* at 380 °C, were outgassed at 350 °C prior to measurements.

Raman spectra were obtained using a Yvon Jobin Horiba (T64000) spectrometer, equipped with a CCD camera detector. As a source of excitation the 514 nm line of a Spectra Physics 2018 Argon/Krypton Ion Laser system were focused through an Olympus BX41 microscope equipped with a 100× magnification objective. The laser power never exceeded 5 mW on the sample.

Transmission electron microscopy (TEM) and scanning transmission electron microscopy (STEM) were performed both in a JEM-2200FS microscope with accelerating voltage of 200 kV. The microscope is equipped with a Schottky-type field emission gun and an ultra high resolution configuration (Cs = 0.5 mm;

Table 1
Nominal and real chemical compositions of catalysts.

Catalysts	Mo _{nom} (atoms/nm ²)	Co/(Co + Mo) _{nom} (atomic ratio)	Mo _{real} (wt.%)	Co _{real} (wt.%)	Mo _{real} (atoms/nm ²)	Co/(Co + Mo) _{real} (atomic ratio)
NT-3-0.3	3	0.3	12.83	3.13	3.52	0.28
NT-4-0.3	4	0.3	13.50	4.73	3.98	0.36
NT-5-0.3	5	0.3	14.98	4.42	4.60	0.32
NT-5-0.2	5	0.2	15.14	3.23	5.03	0.26
NT-5-0.4	5	0.4	15.40	7.2	5.68	0.43

Cc = 1.1 mm; point-to-point resolution = 0.19 nm) and in-column omega-type energy filter. STEM is particularly useful in nanoparticles studies by using a high angle annular dark field (HAADF) detector, which collects electrons that undergo Rutherford scattering; thus, the image can be acquired where the intensity is approximately proportional to Z^2 (Z being the atomic number of the scattering atom). Therefore, elements with a high Z show higher intensities and a white contrast in the image should occur. This technique is useful to distinguish the presence of different chemical elements, when there is a large difference among their atomic numbers, such as in supported catalysts.

Local chemical analysis by energy dispersive X-ray spectroscopy (EDXS) was performed in a NORAN energy dispersive X-ray spectroscope, which is attached to the microscope using the STEM-EDX combination. The samples were ground, suspended in isopropanol at room temperature, and dispersed with ultrasonic agitation, then, an aliquot of the solution was dropped on a 3 mm in diameter lacey carbon copper grid.

X-ray photoelectronic spectroscopy (XPS) on sulfided catalysts was determined in a THERMO-VG SCALAB 250 spectrometer equipped with $Al_{K\alpha}$ X-ray source (1486.6 eV) and a hemispherical analyzer. Experimental peaks were decomposed into components using mixed Gaussian–Lorentzian functions and a non-linear squares fitting algorithm and a Shirley background subtraction was applied. An area ratio of 2/3 and a splitting of 3.2 eV were used to fit the Mo 3d peaks. Binding energies were reproducible to within ± 0.2 eV and the C 1s peak at 284.6 eV was used as a reference from adventitious carbon. Surface elemental composition was determined by fitting and integrating the Co 2p, Mo 3d, S 2p, O 1s and Ti 2p bands and converting these values to atomic ratios using theoretical sensitive factor provided by the manufacturer of the XPS apparatus [26]. All XPS curves are shown with the differential fitting curve (lowest curve in each spectra) after adjusting to theoretical curves. All manipulation of sulfided samples was done under inert conditions using a glovebox and a special box vessel, attached to the XPS equipment, to introduce samples into the ultra high vacuum chamber of the spectrometer.

3. Results and discussion

Chemical compositions determined by AAS on the calcined catalysts are shown in Table 1. In all cases real Mo and Co concentrations were quite close to the nominal ones.

Initially nanotubular support calcined at 400 °C showed SSA of 236 m²/g (Table 2). After impregnation and calcination, SSA and pore volume of the materials decreased slightly in comparison with the single support because of the impregnation of non-porous CoMo precursors and also because of structural changes of the carrier after calcinations [27]. As expected, the catalysts of higher Co and Mo concentration showed lower pore volume and pore size. From the SSA and real Mo loading, the real surface concentration after calcination was between 3.5 and 5.68 atoms/nm², as indicated in Table 1.

Table 2

Textural properties and real Mo surface concentration of supports and catalysts after calcinations.

Support/catalysts	SSA (m ² /g)	TPV (cm ³ /g)	APS (nm)
NT ^a	236	0.52	6.8
NT-3-0.3	229	0.45	6.6
NT-4-0.3	213	0.38	5.8
NT-5-0.3	204	0.39	7.3
NT-5-0.2	189	0.35	6.1
NT-5-0.4	170	0.32	6.2

^a Annealed at 400 °C. SSA: specific surface area, TPV: total pore volume, APS: Average pore size.

3.1. Chemical structure of calcined CoMo/NT catalysts

Raman spectra of support and calcined catalysts are shown in Fig. 1. It is worth starting with the characteristics of the single support before the incorporation of Mo and Co where the typical bands of anatase were evident on the support calcined at 400 °C, particularly the band at 156 cm⁻¹ corresponding to the E1g vibration. [28]. Other bands corresponding to anatase phase at 200, 400, 505, and 640 cm⁻¹ were less intense and broad on the impregnated samples, merging with those of nanotubular structure at 278, 450 and 700 cm⁻¹ [17,29]. Then, after calcination the structure of the nanotubular support is made up of a mixture of anatase and orthorhombic layered phases, suggesting the formation of anatase domains in some regions of the nanotubes walls, as reported elsewhere [22]. Apparently, the incorporation of CoMo on nanotubes stabilizes the orthorhombic structure of layered titanates with nanotubular morphology against its transformation into anatase. In fact, the E1g vibrating mode of anatase decreased in intensity as the amount of Mo and Co loaded increased. Beside the E1g band, two broad bands were observed around 660 and 935 cm⁻¹. The broad peak at 935 cm⁻¹, is likely to be the vibrating mode of terminal Mo=O in tetrahedral coordination [30]. The intensity of the broad band around 660 cm⁻¹ increased considerably compared with those at 278 and 450 cm⁻¹, then, the major contribution to the band 660 cm⁻¹ comes from the oxidized CoMo phase, suggesting the presence of a well dispersed β -CoMoO₄ phase [31,32] in all the samples, regardless of the amount of Mo loaded (at constant Co/(Co + Mo) = 0.3 atomic ratio).

The optimization of the Co/(Co + Mo) atomic ratio was examined on a high Mo loaded catalyst (e.g., 5 atoms/nm²). The Mo species loaded on the NT support strongly depend on the amount of Co loaded, as shown in Fig. 2. At Co/(Co + Mo) = 0.2, additional to the broad bands at 660 and 935 cm⁻¹, two narrow bands were observed at 815 and 990 cm⁻¹, corresponding to the Mo–O–Mo vibration and to terminal Mo=O in MoO₃ particles, respectively [33,34]. Other less intense bands at 125, 243, 288 and 335 cm⁻¹ confirm the presence of MoO₃ phase. At higher Co loading, (sample NT-5-0.4), the intensity of the band at 935 cm⁻¹ increased considerably, in comparison with that in NT-5-0.3, suggesting a well defined CoMoO₄ phase or an increase on the crystallite dimension of CoMoO₄ phase dispersed on this sample. These results can be rationalized as follows: At low Co loading, (e.g., NT-5-0.2), there are not enough Co atoms to react with all loaded Mo, then, a fraction of Mo segregates as MoO₃, while the rest reacts with Co forming CoMoO₄ phase. At high Co loading (e.g.,

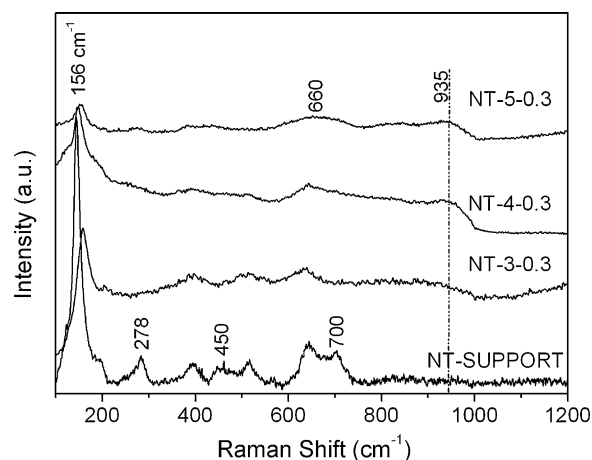


Fig. 1. Raman spectra of support and calcined CoMo/NT catalysts, with different Mo loadings at constant Co/(Co + Mo) = 0.3 atomic ratio.

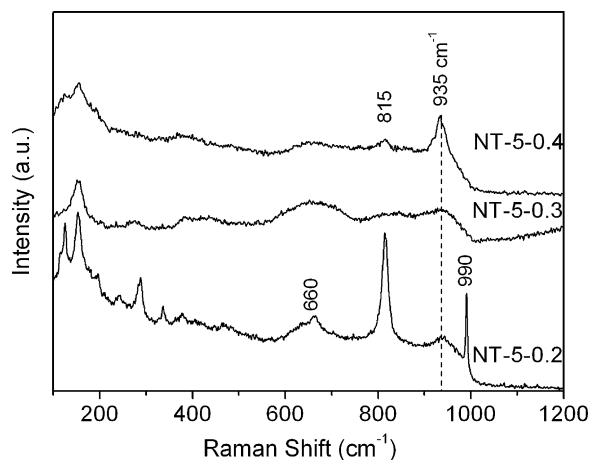


Fig. 2. Raman spectra of calcined CoMo/NT catalysts, at constant Mo loading 5 atoms/nm², with different Co/(Co + Mo) atomic ratio.

NT-5-0.4), there are more Co atoms available to react with Mo, and larger or well defined crystallites of CoMoO₄ phase are produced. The optimum Co/(Co + Mo) atomic ratio was fixed at 0.3, where well-dispersed CoMoO₄ phase was obtained. Then, using the HRTEM technique the dispersion of the mixed oxide phase CoMoO₄, was studied in detail in the following electron microscopy analysis.

3.2. MoS₂ particles morphology

HRTEM technique has been used to study the orientation of MoS₂ crystallites on catalyst supports, mostly on γ -Al₂O₃, widely used as HDS support. As is shown in Fig. 3a, nanotubular features of NT support were maintained after CoMo impregnation in NT-5-0.3 and after annealing at 380 °C. Small white dots dispersed homogeneously on the walls of the nanotubes are observed in the HAADF image of Fig. 3b. As the HAADF detector collect electrons, that experiments Rutherford scattering, then, the white dots on the walls of TiO₂ nanotubes correspond to Co and Mo in the CoMoO₄ phase. The reason is that the scattered electron intensity from the sample is directly proportional to square of atomic number. So, the scattered electrons from the Co and Mo atoms are intenser than those from Ti and O atoms. This phenomenon was previously reported for tungsten nanoparticles deposited on a similar NT-support [23]. The size of these nanoparticles was measured on several white dots by using the intensity profiles and it was below 3 nm.

In NT-5-0.2 (see Fig. 3c), with low Co concentration, two kinds of Mo species were observed: One corresponds to Co and Mo atoms in CoMoO₄ nanoparticles homogeneously smeared on the surface of the nanotubes, size below 3.0 nm, as determined in sample NT-5-0.3. The second one corresponds to large particles (see inset in Fig. 3c), which were mainly made up by molybdenum atoms, as determined by EDXS analysis (not shown). Therefore, these large particles correspond to well crystallized and segregated MoO₃ in agreement with our previous Raman spectroscopy results (see

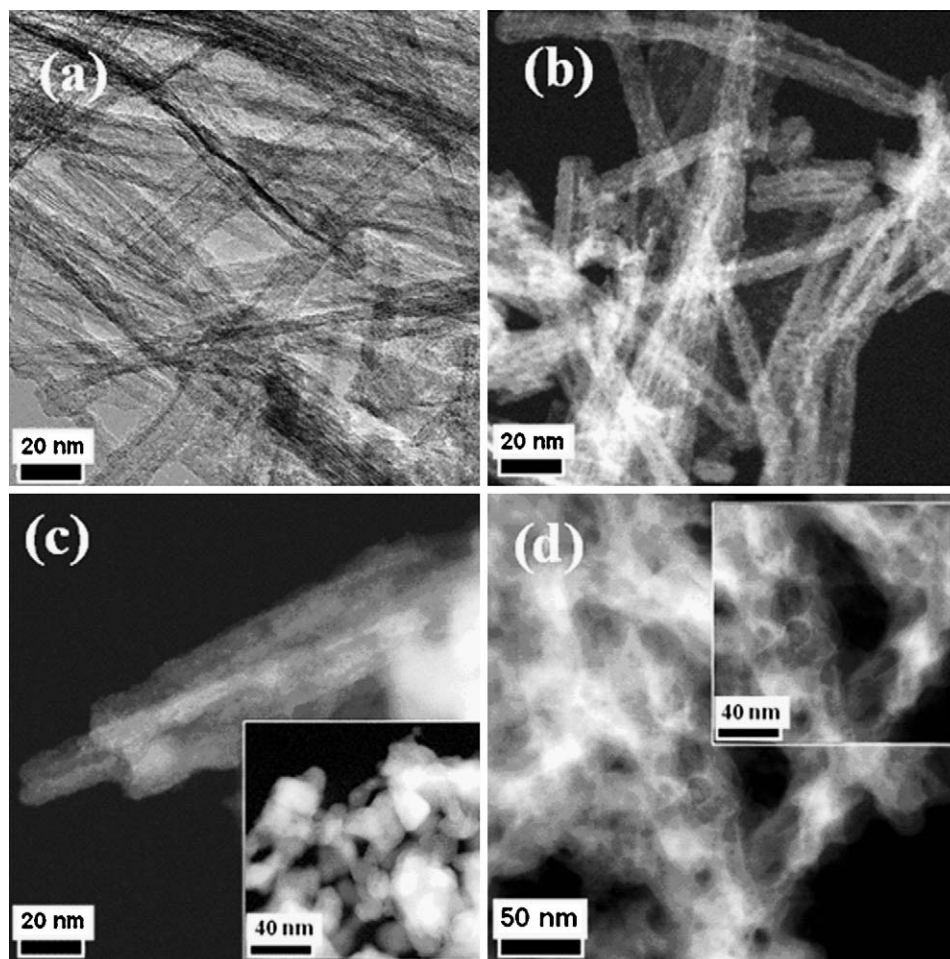


Fig. 3. (a) Bright field TEM image of oxidized CoMo/NT: NT-5-0.3. HAADF image of oxidized CoMo/NT in (b) NT-5-0.3, (c) NT-5-0.2 and (d) NT-5-0.4.

Fig. 2). When the amount of Co increased (e.g., in NT-5-0.4), where more crystalline CoMoO_4 phase was detected by Raman spectroscopy (see Fig. 2), the nanotubular support appeared embedded into a polymeric matrix constituted of CoMoO_4 phase. Notice that the whole scanning area in the HAADF image (Fig. 3d) was highlighted in a white polymeric matrix in which the nanotubes of TiO_2 are embedded, as determined by EDXS analysis (not shown).

Structural and morphological features of the single NT support have been discussed in detail elsewhere [22,35]. But a representative HRTEM image is presented in Fig. 4a in order to set forth a

starting morphology of the support. The nanotubes are composed by 3 or 4 structural layers, with an inner diameter of 5.5 nm and an outer one of about 10 nm. After impregnation of the CoMoS precursors, the nanotubular morphology of support remained unchanged, with MoS_2 slabs distributed along the nanotubes, as shown in Fig. 4b–f. At low Mo loading (e.g., NT-3-0.3) in Fig. 4b, short MoS_2 slabs composed by just two layers were observed. As expected, the density of the MoS_2 layered structure increased with Mo loading in NT-4-0.3, as shown in Fig. 4c. However, no indication of a higher stacking level than two was observed at this Mo loading.

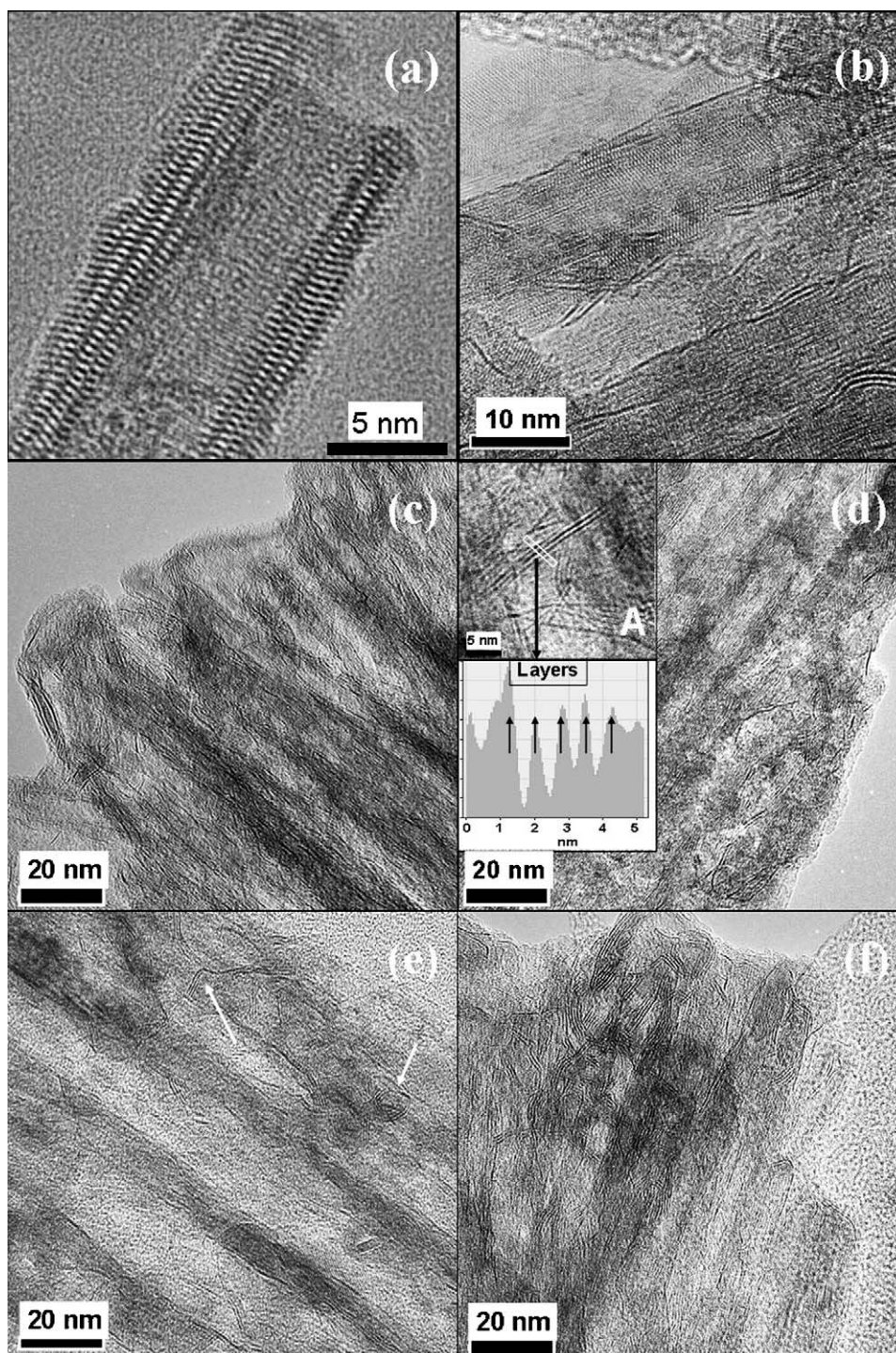


Fig. 4. HRTEM images of (a) NT support calcined at 400 °C. TEM images of (b) NT-3-0.3, (c) NT-4-0.3, (d) NT-5-0.3, inset A higher magnification of MoS_2 layers where the layers number are displayed in intensity profile, (e) NT-5-0.2 and (f) NT-5-0.4.

When Mo concentration increased to 5 atoms/nm² in NT-5-0.3, the stacking level of MoS₂ slab increased between 3 and 6 structural layers with an interlayer spacing of 0.61 nm, as indicated in intensity profile inset A, in Fig. 4d. The length of the MoS₂ slabs also increased considerably in comparison with NT-3-0.3 and NT-4-0.3, as depicted in Fig. 4b and c, respectively. Similar MoS₂ features were observed for NT-5-0.2 and NT-5-0.4 samples, Fig. 4e and f, although in some regions, the long MoS₂ slabs were curved producing onion-like or inorganic fullerene-like nanostructures, see Fig. 5, as those obtained after sulfiding bubbles of MoO₃ at 800 °C, as reported by Tenne [20,21]. A magnified HRTEM image of a curved structure of MoS₂ slabs is shown in Fig. 5b. Large MoS₂

layers and high stacking in the catalyst of high Mo loading were observed, as shown in Fig. 5a–c. Also in this case, markedly curved structures were detected indicating a low interaction of Mo species with the nanotubular support, as observed in commercial type 2 CoMoS/or NiMoS/Al₂O₃ catalysts [24]. Sakashita et al. observed edge-bonded MoS₂ crystallites species on anatase, and attributed the cause to an epitaxial relationship between MoS₂ and the anatase surface [36]. These observations indicate that the orientation and morphology of the MoS₂ catalysts strongly depend on the crystal plane on the surface of the support [36,8]. However, the study of Sakashita et al. was carried out on a 3.3 wt.% Mo catalyst [36]; a low amount in comparison with industrial catalysts

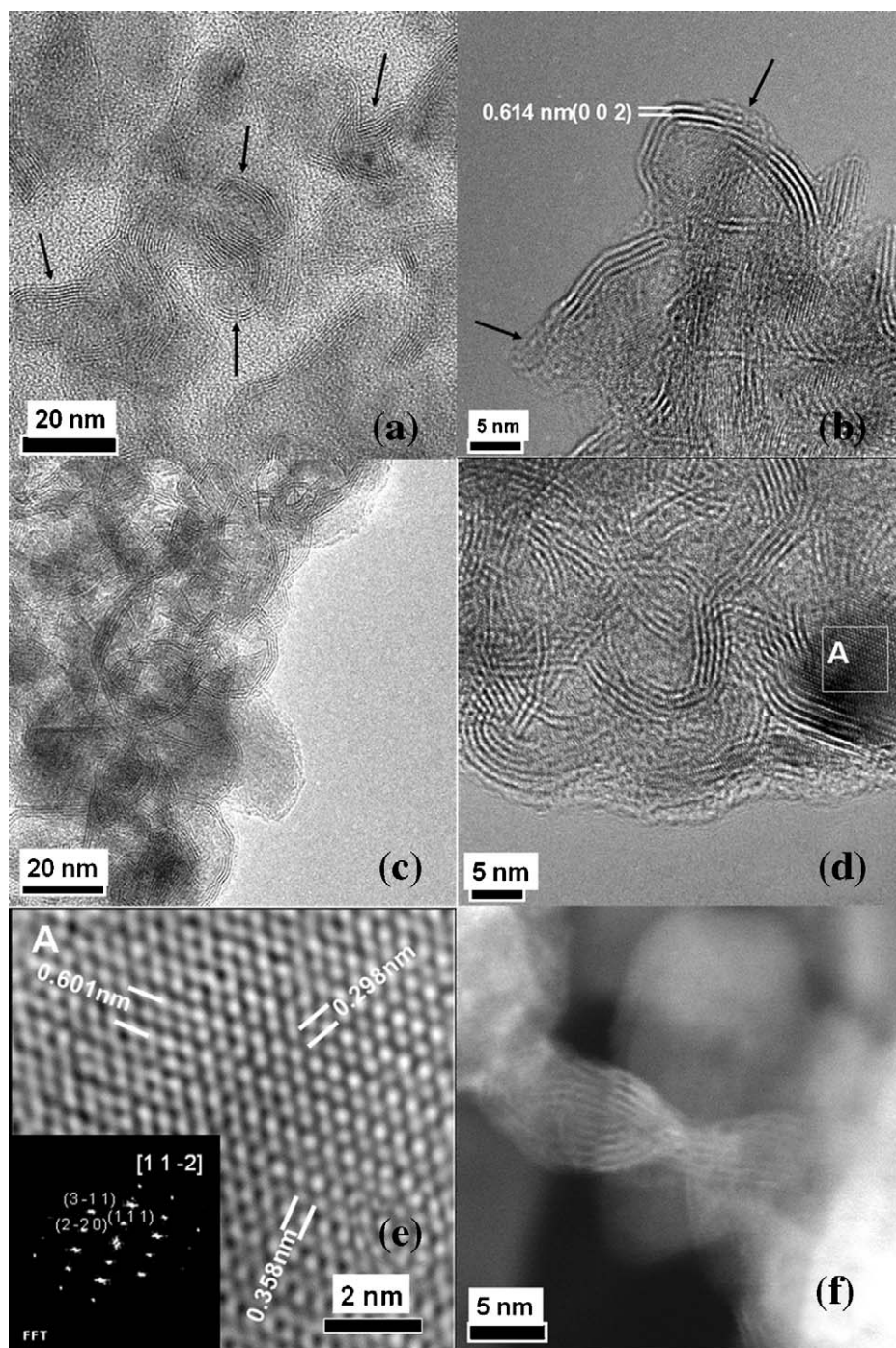


Fig. 5. HRTEM images. (a) NT-5-0.2, (b) NT-5-0.3, (c) NT-5-0.4, (d) high magnification image of NT-5-0.4, (e) high magnification of region A of (d) and its Fourier transform and (f) HAADF image of NT-5-0.3 sample showing a tridimensional image of almond seed like particles.

(e.g., ~12 wt.%) which require higher concentrations of Mo to attain better HDS efficiency. Likely, higher Mo loadings may lead to larger MoS₂ slabs lying on their basal planes.

Additionally, some isolated regions of fullerene-like MoS₂ were observed in the catalysts of the highest Mo content. The density of these nanostructures markedly depended on the Co/(Co + Mo) atomic ratio, as shown in Fig. 5. At Co/(Co + Mo) = 0.2, some fullerene-like structures with 3 or 4 stacking level were observed in Fig. 5a, marked by black arrows. At this Co content, a large amount of MoO₃ was segregated as indicated by our Raman results in Fig. 2. However, MoO₃ particles remained well dispersed on the nanotubular support. After sulfidation, MoO₃ nanoparticles transformed into fullerene-like nanostructures. At higher Co loading (e.g., NT-5-0.3), these isolated MoS₂ nanostructures were less frequently observed, as shown in Fig. 5b with fullerene-like structures made up of 3 or 4 layers; as shown in Fig. 2, in this sample CoMoO₄ phase was highly dispersed. Apparently, the outer layer is dislocated and became amorphous, which could be an indication of the Co inclusion on the edges of MoS₂ slabs forming then the CoMoS phase, black arrows in Fig. 5b. In NT-5-0.4, where well defined CoMoO₄ phase was observed by Raman (see Fig. 2), a large amount of fullerene-like MoS₂ particles composed by 4–6 slabs were detected (see Fig. 5c and d). It is well known that sulfidation of CoMoO₄ phase generates into separate Co₉S₈ and MoS₂ phases, and null or low promotion effect of Co on the MoS₂ phase is attained to generate the CoMoS phase [37,38]. A similar result was found on NT-5-0.4 where Co-rich Mo particles were present in the fullerene-like MoS₂ particles as illustrated in Fig. 5d, inset A. HRTEM image was obtained from the region marked by “inset A” in Fig. 5d and it is displayed in Fig. 5e, where 0.601, 0.358 and 0.298 nm interplanar distances and derived Fourier transform (FT) were measured. Crystallographic analysis from FT indicated that these distances correspond to the (1 1 1), (2–2 0) and (3–1 1) planes of the cubic Co₉S₈ phase according to the JCPDS card No. 86-2273. It should be noted that in this case the Co/Mo molar ratio of oxidized precursor phase (~0.66) is not very far from the stoichiometric for the CoMoO₄ phase. Sulfidation of this phase results in segregated Co₉S₈ crystallites and curved MoS₂ structures are mainly formed, as previously reported for unsupported sulfided CoMoO₄ phase [37]. In NT-5-0.3, the segregation of Co₉S₈ phase was not observed. In this case, the MoS₂ nanoparticles had ellipsoidal morphology yielding almond seed-like MoS₂ nanoparticles, with 4 or 6 curved slabs, and interlayer distance of 0.614 nm as shown in Fig. 5b. The top layer of MoS₂ structure appeared interrupted or dislocated suggesting that Co atoms are located at the edge sites of MoS₂ particles. Accordingly, HAADF-STEM have been used to study the change in morphology on triangular clusters containing only a S–Mo–S layer with addition of promoting atoms like Co or Ni [39,40], where a triangular morphology of MoS₂ clusters showed higher truncation degree when Co atoms were added exposing extended high index [1120] truncation. A high resolution HAADF image of a Co–Mo–S nanoparticle in NT-5-0.3 is showed in Fig. 5f. As aforementioned, the sulfided nanoparticle has an almond seed-like morphology, composed by several MoS₂ slabs.

3.3. Sulfidability of surface species in CoMoS/NT catalysts

XPS spectra from Mo 3d, Co 2p and S 2p signals for the different NT catalysts are plotted in Figs. 6–8. The Mo 3d signal was fitted by considering the following species: (i) Mo⁴⁺ from completely sulfided MoS₂, (ii) Mo⁵⁺ from molybdenum oxy-sulfides and (iii) Mo⁶⁺ from unreduced molybdenum oxide [41,42].

Co 2p spectra was fitted with four doublets: (i) The one occurring at 778.5–779.7 from sulfided Co–S, (ii) another one at 781.5–781.9 from oxidized Co–O and (iii) the other two broad

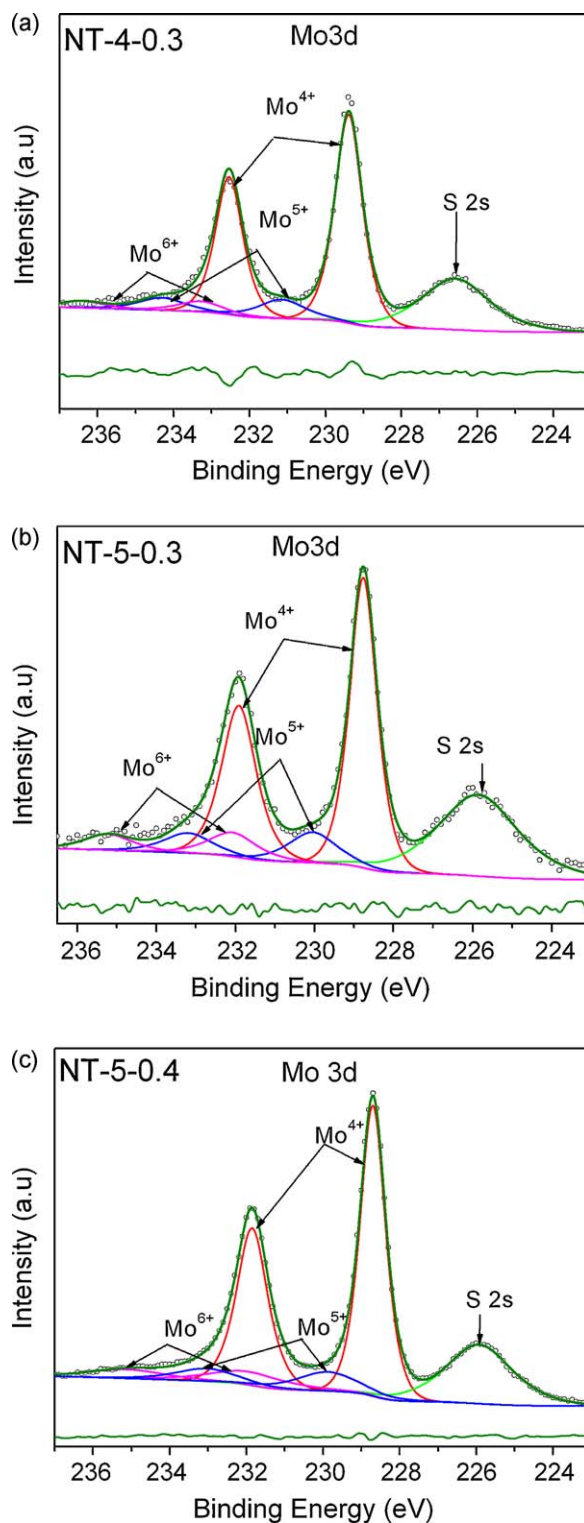


Fig. 6. Representative XPS of: Mo 3d spectrum from CoMo/NT Sulfided samples.

doublets arise from two satellite signals, as shown in Fig. 7, in agreement with literature elsewhere [43–45].

The surface composition, binding energy (BE) and full width at half maximum (FWHM) values of the different components are reported in Tables 3 and 4, respectively. FWHM values around 1.0 eV suggest that the XPS signal is made up of only one contribution or oxidation state of each component. As can be noticed, total Mo and Co dispersion increased along Mo loading.

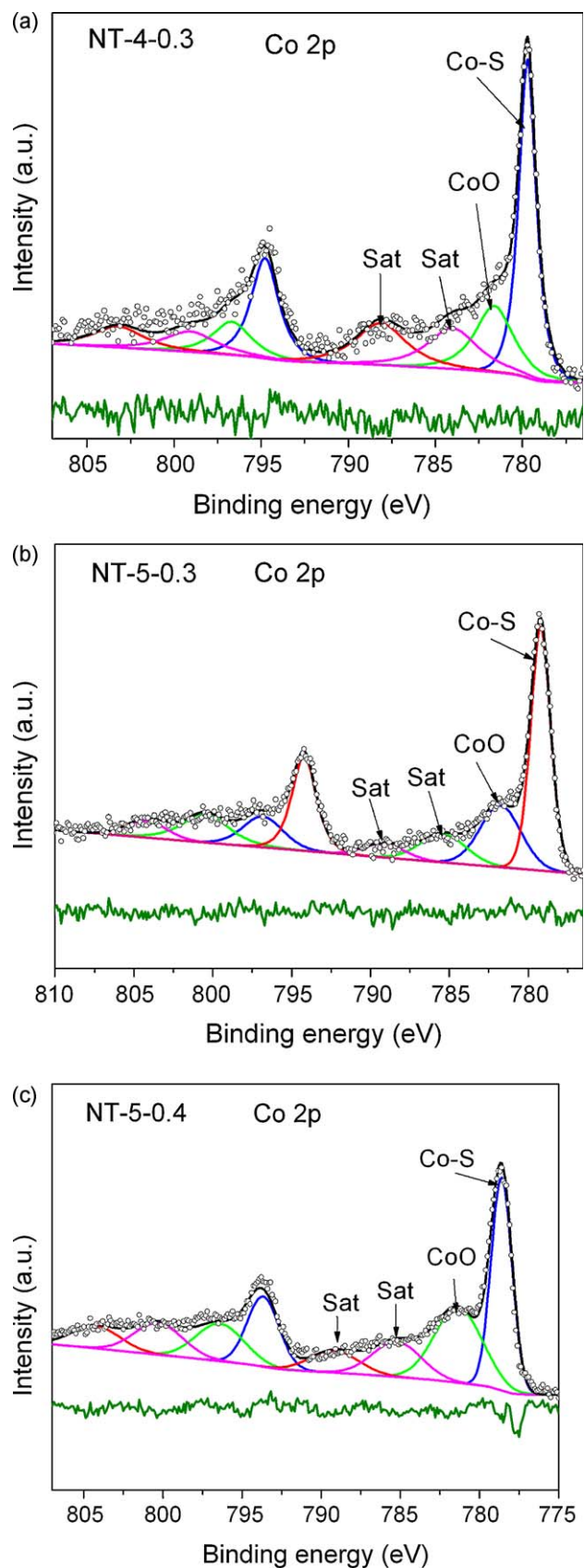


Fig. 7. Representative XPS of: Co 2p spectrum from CoMo/NT Sulfided samples.

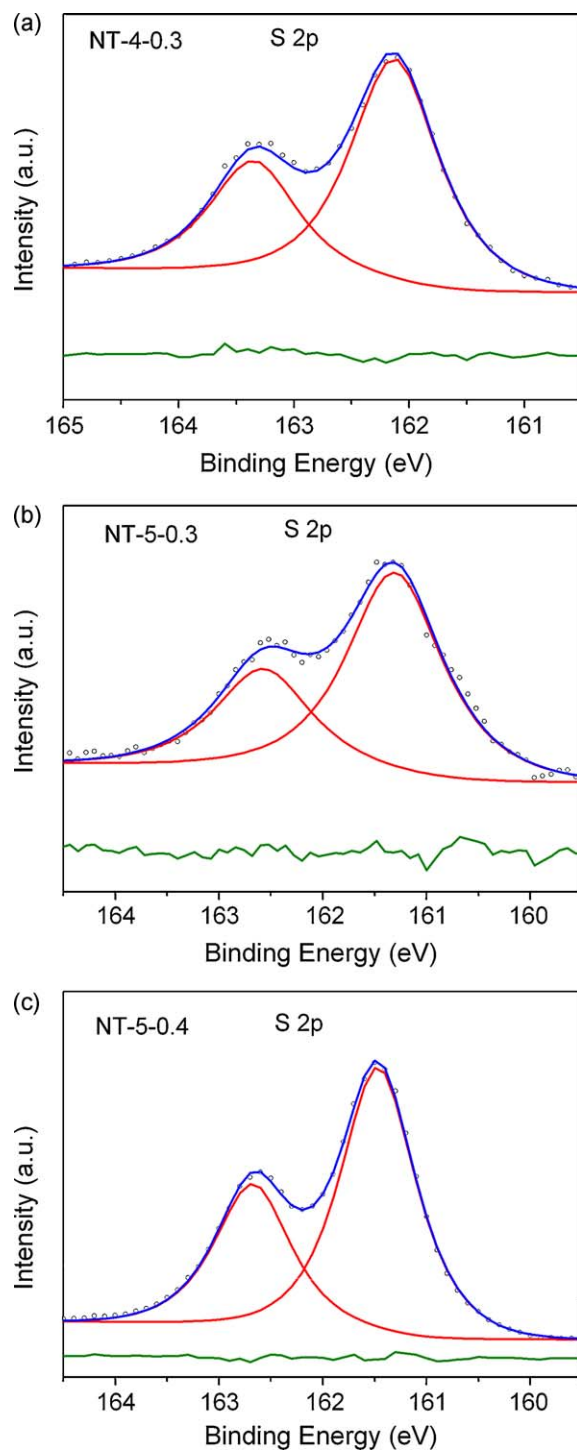


Fig. 8. Representative XPS of: S 2p spectrum from CoMo/NT Sulfided samples.

When increasing Mo loading from 3 to 5 atoms/nm² and keeping a constant Co/(Co + Mo) ratio at 0.3, sulfided Mo⁴⁺ increased from 5.8 to 11.6 at.% and sulfided Co-S increased from 1.3 to 2.7 at.%, respectively; both components increased by a factor of 2.3, suggesting that, even in samples of high metal loading, Co and Mo sulfided species are efficiently dispersed on the nanotubular support. The effect of the Co/(Co + Mo) atomic ratio was studied in the catalysts of the highest Mo loading where sulfided Mo⁴⁺ was 13.6 and 15.0 at.%, as indicated in Table 3. The Co-S concentration strongly depended on the Co/(Co + Mo) ratio, showing a maximum for the sample where that ratio was 0.3 (NT-5-0.3).

Table 3

Atomic chemical composition (as determined by XPS) of sulfided catalysts.

Catalyst	Surface chemical composition (at.%)								
	S	Ti	Co _{tot}	Co–S ^a	Co–O ^b	Mo _{tot}	Mo ⁴⁺	Mo ⁵⁺	Mo ⁶⁺
NT-3-0.3	17.8	27.9	2.83	1.34	1.49	8.7	5.79	1.38	1.53
NT-4-0.3	15.6	22.5	4.77	2.54	2.23	12.93	10.45	1.62	0.86
NT-5-0.3	16.8	19.3	4.06	2.76	1.30	14.24	11.64	1.23	1.41
NT-5-0.2	17.4	18.3	3.81	1.62	2.19	21.12	13.63	4.11	3.38
NT-5-0.4	20.3	21.6	5.61	2.38	3.23	19.51	15.03	2.09	2.39

^a Sulfided Co.^b Oxidized Co.

Mo 3d_{5/2} BE for sulfided Mo⁴⁺ species remained close at 228.8 ± 0.2 eV for all the samples (see Table 4) in agreement with BE value reported for MoS₂ phase [46]. The Co 2p_{3/2} BE was around 779.3 eV for samples with Co/(Co + Mo) = 0.3. This value shifted to 778.9 and 778.6 eV when the Co/(Co + Mo) varied from 0.2 to 0.4, respectively. Accordingly, the BE value reported for segregated Co₉S₈ phase is around 778.5 eV [47,48]. On the other hand, when Co species chemically interact with the edge sites of MoS₂ particles (to form the “CoMoS” phase), BE shifts to a value ~0.9 eV higher than that for Co₉S₈. Then, the results shown in Table 4 strongly suggest that Co species impregnated at Co/(Co + Mo) = 0.3 (in the final catalyst) give rise to sulfided species in intimate interaction with MoS₂ particles, in comparison with those obtained in materials at Co/(Co + Mo) = 0.2 or 0.4. Based on these facts, it can be assumed that a higher amount of “CoMoS” phase is formed when Co and Mo are deposited at Co/(Co + Mo) = 0.3. Presumably, at this condition, good promotion of MoS₂ by Co could be achieved.

These results can be rationalized as follows: (i) at low Co concentration, Co/(Co + Mo) = 0.2, the amount of Co available to react with Mo atoms is too low (Co/Mo = 0.25) to form appreciable amounts of CoMoO₄ (the precursor of CoMoS phase) and hence, some MoO₃ segregates. Thus, after sulfiding just a little amount of promoted phase was observed. (ii) At high Co concentration, Co/(Co + Mo) = 0.4, (Co/Mo = 0.66), closer to the CoMoO₄ stoichiometric atomic ratio, more CoMoO₄ was observed in Raman spectra and during sulfidation; Co₉S₈ segregates and curved MoS₂ particles were mainly formed. Then, Co/(Co + Mo) = 0.3, (Co/Mo = 0.5), is the optimum atomic ratio to generate a well promoted CoMoS phase on our nanotubular support. These facts should be reflected in enhanced HDS activity.

Representative S 2p spectra of different catalysts are presented in Fig. 8. Except for the catalyst with the lowest metal loading (e.g., NT-3-0.3) all spectra were fitted with just one S 2p doublet, having

a S 2p_{3/2} BE of 161.5 ± 0.3 (See Table 4) corresponding to S^{2−} ions in MoS₂ in agreement with literature [49]. The spectrum of NT-3-0.3 (not shown), was made up of two broad peaks, that were fitted with two doublets revealing the presence of at least two sulfur species, associated to S^{2−} and S₂^{2−} ligands [41,43].

The sulfidability of Co increased from 47.3 to 68.0 as nominal Mo loading rose from 3 to 5 atoms/nm², at Co/(Co + Mo) = 0.3, as indicated in Table 5. At higher Mo loadings, a large amount of edge sites is available to be promoted by Co atoms upon sulfidation (see column 8 Table 3). Then, Co sulfidability increased. When Co/(Co + Mo) was varied from 0.3 to 0.2 or to 0.4, Co sulfidability decreased from 68% to 42%, respectively. At low atomic ratio, large crystallites of MoO₃ segregate (see Raman and TEM results, Figs. 2 and 5, respectively), being difficult to sulfide. In fact, Mo sulfidability dropped. Since there are not enough edge sites to be promoted, Co atoms aggregates in oxidized species decreasing also its sulfidability. In contrast, at high atomic ratio, sulfided Co atoms aggregates into large Co₉S₈ crystallites, as observed by HRTEM (Fig. 5e), and sulfidability decreased considerably as determined by XPS.

The S/(CoS + MoS) atomic ratio, as determined by XPS, was around 1.2–1.5 (see column 4, Table 5). Only in the catalyst with the lowest metal loading, NT-3-0.3, the ratio was over 2. As aforementioned, two different sulfur species were detected (spectrum not shown) in this sample.

Co and Mo surface coverage was estimated by the surface atomic ratio (Co + Mo)/(Co + Mo + Ti), from the total amount of Co and Mo atoms determined in the corresponding XPS spectra. As indicated in Table 5 (column 5), overall Co and Mo dispersion increased from 0.3 to around 0.5 for nominal Mo loadings of 3 and 5 atoms/nm², respectively. However, not all the Co and Mo atoms exposed on the surface are sulfided, then, the amount of sulfided species dispersed on the surface can be determined by the atomic ratio [(CoS + MoS)/(Co_{tot} + Mo_{tot} + Ti)] also reported in Table 5 (see column 6). As expected, the amount of sulfided Co and Mo species dispersed on the surface increased as metal loading increased. Nevertheless, it is necessary to point out that not all the sulfided Co and Mo species are forming the active CoMoS phase. The CoS/MoS atomic ratio also presented in Table 5 represents the promotion factor of MoS₂ by Co atoms to yield the CoMoS phase. The promotion factor was 0.23 ± 0.01 for samples synthesized with a Co/(Co + Mo) = 0.3, whereas this (CoS/MoS) atomic ratio decreased considerably in samples prepared with Co/(Co + Mo) = 0.2 or 0.4.

Noteworthy, samples prepared at Co/(Co + Mo) = 0.3 showed the same Co–S BE (779.3 eV) and same promotional factor (CoS/MoS = 0.24) as reported in Table 5, whereas in samples where the Co/(Co + Mo) was 0.2 and 0.4, that is, NT-5-0.2 and NT-5-0.4, the promotional factor decreased to 0.12 and 0.16, respectively, and the BE position was similar to that reported for Co₉S₈ (778.5 eV). Multiplying the dispersion of sulfided species (CoS + MoS)/(Co_{tot} + Mo_{tot} + Ti) by the promotional factor (CoS/MoS) allowed us to propose a procedure to calculate the density of CoMoS phase on the surface of nanotubular titania (δ), regardless of the Co/

Table 4

Binding Energy and FWHM values of atomic components of sulfided catalysts.

Samples	Binding Energy (eV)/FWHM (eV) ^a			
	S (2p)	Ti (2p _{3/2})	Co (2p _{3/2}) ^b	Mo (3d _{5/2}) ^c
NT-3-0.3	161.2	458.9	779.3	228.6
	1.7	1.4	1.4	0.95
NT-4-0.3	161.7	459.3	779.3	229.0
	0.92	1.2	1.2	0.87
NT-5-0.3	161.7	459.3	779.3	228.9
	0.92	1.2	1.5	0.83
NT-5-0.2	161.6	459.1	778.9	228.9
	0.83	1.2	1.6	0.82
NT-5-0.4	161.5	458.9	778.6	228.7
	0.88	1.2	1.4	0.80

^a Full width at half maximum.^b Sulfided Co.^c Sulfided Mo.

Table 5

Surface chemical composition of sulfides Co and Mo atoms derived from XPS measurements.

Catalyst	Sulfidation (%)		S/(CoS + MoS) (atomic ratio)	Co + Mo/[Co + Mo + Ti] (atomic ratio)	CoS + MoS/[Co + Mo + Ti] (atomic ratio)	CoS/MoS	δ^a
	Co	Mo					
NT-3-0.3	47.3	66.6	2.5	0.29	0.18	0.23	0.041
NT-4-0.3	53.2	80.8	1.2	0.44	0.32	0.24	0.076
NT-5-0.3	68.0	81.5	1.2	0.49	0.38	0.24	0.091
NT-5-0.2	42.5	64.5	1.2	0.58	0.35	0.12	0.042
NT-5-0.4	42.4	77.0	1.2	0.54	0.37	0.16	0.059

^a CoMoS phase density.

(Co + Mo) ratio and on the Mo loading, which linearly correlated with the pseudo first order kinetic constant in the DBT HDS as shown in the following section.

By varying Co loading in samples of high Mo concentration no significant morphological changes in highly stacked MoS₂ particles (Fig. 5a–c) were evident. On the other hand, CoMoS phase density clearly decreased (see column 8 in Table 5) when the Co/(Co + Mo) ratio did not correspond to the optimal value (0.3). Thus, δ and MoS₂ stacking are likely to be independent parameters, even though both increased with Mo and Co loading (samples at (Co + Mo) = 3, see column 8 in Table 5 and Fig. 4b–d).

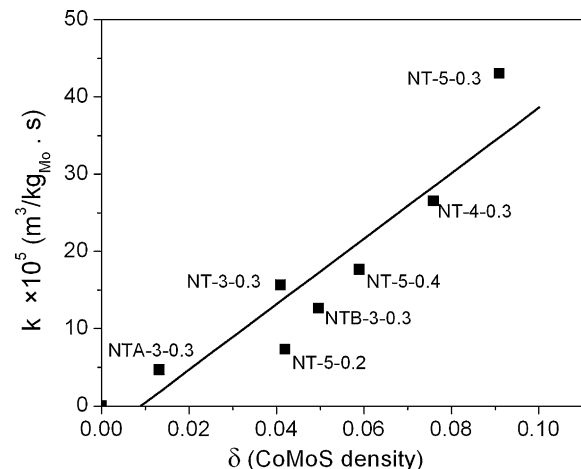
3.4. HDS on CoMoS/NT catalysts

HDS catalytic activity of CoMoS/NT catalysts on DBT is reported in Table 6. HDS activity increased with Mo loading, at constant Co/(Co + Mo) = 0.3, suggesting that all the metal loading was uniformly dispersed on the nanotubular support. However, when Co/(Co + Mo) varied, to 0.2 and to 0.4, the HDS activity decreased considerably. Clearly these differences in catalytic activity correlate with the density (δ) of CoMoS phase determined by XPS. In fact, from Fig. 9, it can be observed that HDS activity is

Table 6

Pseudo-first order kinetic constant, DBT HDS over various sulfided CoMo catalysts supported on nanostructured titania.

Catalyst	$k \times 10^3$ (m ³ /kg _{cat} s)	$k' \times 10^5$ (m ³ /kg _{Mo} s)
NT-3-0.3	2.00	15.6
NT-4-0.3	3.58	26.5
NT-5-0.3	6.44	43.0
NT-5-0.2	1.11	7.3
NT-5-0.4	2.71	17.6

Batch reactor, 320 °C, 56 kg/cm², 1000 rpm mixing speed, *n*-hexadecane as solvent.**Fig. 9.** Reaction kinetic constant of HDS of DBT as function of CoMoS phase density (δ) determined by XPS.

directly proportional to δ , the density of CoMoS phase generated on the surface of NT.

To construct the linear plot in Fig. 9, XPS and catalytic activity of two samples prepared at different acid and basic pH NTA-3-0.3 and NTB-3-0.3, respectively, were included [25]. These catalysts have the same Mo loading and Co/(Co + Mo) atomic ratio, but were obtained through different methods (see [25] for details in materials preparation). Then, it can be concluded that, regardless of the different preparation conditions, HDS of DBT strongly depends on the surface density of CoMoS phase, e.g., δ .

In fact, a direct correlation can be established between the CoS and sulfided Mo⁴⁺ determined by XPS and the HDS activity, suggesting that higher dispersion in CoS and MoS₂ correspond to higher HDS activity. Moreover, as aforementioned, the BE of Co–S in NTA-3-0.3 occurred at 779.0 eV suggesting that most of the Co atoms are not in close interaction with MoS₂ [25]. Thus, in this case the formation of the “CoMoS” was limited and its corresponding HDS activity was low. Meanwhile, in the other samples (NTB-3-0.3 and NT-3-0.3) the Co–S BE shifted to 779.3 eV suggesting a more efficiently promoted MoS₂ phase, this fact being well-correlated with their enhanced HDS activity [25].

According to Fig. 9, the main factor determining HDS activity of various materials is their concentration of CoMoS phase. The linear trend found when plotting these parameters indicate that the nature of active sites present in different materials is similar; the amount of CoMoS phase dictating the catalytic behavior. The available information precludes discrimination between sites type 1 and 2 on our materials, although the high stacking degree observed for samples of high Mo loading (Fig. 4d–f) strongly suggests molybdenum sulfide particles in low interaction with the nanotubular support (e.g., type 2 sites, [50]). Formation of fullerene-like or onion-like MoS₂ particles also point out in that direction (see Fig. 5). Thus, in our materials, type 2 sites are likely to be present even in the case of catalysts of moderate Mo loading (3 atmos/nm² nominal surface concentration).

4. Conclusions

Fullerene-like CoMoS and MoS₂ nanoparticles were found dispersed along nanotubular TiO₂. Differently from other CoMoS particles supported on γ -Al₂O₃ or anatase TiO₂, where hexagonal CoMoS and/or MoS₂ particles have been clearly identified, in nanotubular TiO₂, curved onion-like particles were observed smeared along the nanotubes. The number of MoS₂ slabs varied from about 2 to 6, depending on the Mo loading. Dislocations in the outer most zones of MoS₂ particles strongly indicate the formation of CoMoS sites, being the corner stone of highly active HDS catalysts. Since not all MoS₂ particles are promoted by Co, a quantification of the CoMoS surface density (δ) was achieved by XPS spectroscopy and then it was correlated with HDS activity. The independent variable Co/(Co + Mo), used in this work to optimize CoMoS formation on nanotubular TiO₂, was varied from 0.2 to 0.4, and Mo loading from 3 to 5 atoms/nm², with a view to approach higher Mo contents as required for highly active industrial HDS

catalysts. A linear correlation between HDS activity of DBT and δ , indicates that the highest CoMoS formation ($@ \text{Co}/(\text{Co} + \text{Mo}) = 0.3$ and $\text{Mo} = 5 \text{ atoms/nm}^2$) in fact results in the most active catalyst of a series, δ being a trustworthy parameter to screen potential HDS catalysts.

Acknowledgment

The authors would like to acknowledge the IMP for the financial support through the projects: IMP-D.00446 and D.00447.

References

- [1] H. Topsøe, B.S. Clausen, F.E. Massoth, J.R. Anderson, M. Boudart (Eds.), *Catalysis Science and Technology*, Springer, Berlin, 1996, p. 11.
- [2] H. Topsøe, B.S. Clausen, *Catal. Rev. Sci. Eng.* 26 (1984) 395–420.
- [3] S. Eijssbouts, *Appl. Catal. A* 158 (1997) 53–92.
- [4] S.M.A.M. Bouwens, F.B.M. van Zon, M.P. van Dijk, A.M. van der Kraan, V.H.J. de Beer, J.A.R. van Veen, D.C. Koningsberger, *J. Catal.* 146 (1994) 375–393.
- [5] M. Breyse, C. Geantet, P. Afanasiev, J. Blanchard, M. Vrinat, *Catal. Today* 130 (2008) 3–13.
- [6] M. Sun, D. Nicosia, R. Prins, *Catal. Today* 86 (2003) 173–189.
- [7] R. Cattaneo, Th. Weber, T. Shido, R. Prins, *J. Catal.* 191 (2000) 225–236.
- [8] H. Shimada, *Catal. Today* 86 (2003) 17–29.
- [9] J. Ramirez, L. Cedeño, G. Busca, *J. Catal.* 184 (1999) 59–67.
- [10] M. Vrinat, D. Hamon, M. Breyse, D. Durand, T. Courieres, *Catal. Today* 20 (1994) 273–282.
- [11] S. Damyanova, L. Petrov, P. Grange, *Appl. Catal. A* 239 (2003) 241–252.
- [12] Y. Saih, M. Nagata, T. Funamoto, Y. Masuyama, K. Segawa, *Appl. Catal. A* 295 (2005) 11–22.
- [13] J. Ramirez, S. Fuentes, G. Díaz, M. Vrinat, M. Breyse, M. Lacroix, *Appl. Catal.* 52 (1989) 211–224.
- [14] S. Inoue, A. Muto, H. Kudou, T. Ono, *Appl. Catal. A* 269 (2004) 7–12.
- [15] S. Dzwigaj, C. Louis, M. Breyse, M. Cattenot, V. Belliere, C. Geantet, M. Vrinat, P. Blanchard, E. Payen, S. Inoue, H. Kudo, Y. Yoshimura, *Appl. Catal. B* 41 (2003) 181–191.
- [16] T. Kasuga, M. Hiramatsu, A. Hoson, T. Sekino, K. Niihara, *Langmuir* 14 (1998) 3160–3163.
- [17] D.V. Bavykin, J.M. Friedrich, A.A. Lapkin, F.C. Walsh, *Chem. Mater.* 18 (2006) 1124–1129.
- [18] G.H. Du, Q. Chen, R.C. Che, Z.Y. Yuan, L.M. Peng, *Appl. Phys. Lett.* 79 (2001) 3702.
- [19] J. Escobar, J.A. Toledo, M.A. Cortés, M.L. Mosqueira, V. Pérez, G. Ferrat, E. López-Salinas, E. Torres-García, *Catal. Today* 106 (2005) 222–226.
- [20] R. Tenne, *Nature* 431 (2004) 640–641.
- [21] R. Tenne, *Angew. Chem. Int. Ed.* 42 (2003) 5124–5132.
- [22] J.A. Toledo-Antonio, S. Capula, M.A. Cortés-Jácome, C. Angeles-Chavez, E. López-Salinas, G. Ferrat, J. Navarrete, J. Escobar, *J. Phys. Chem. C* 111 (2007) 10799–10805.
- [23] M. Cortés-Jácome, M. Morales, C. Angeles-Chávez, L.F. Ramírez-Verduzco, E. López-Salinas, J.A. Toledo Antonio, *Chem. Mater.* 19 (2007) 6605–6614.
- [24] S. Eijssbouts, L.C.A. van den Oetelaar, R.R. van Puijenbroek, *J. Catal.* 229 (2005) 352–364.
- [25] M.A. Cortés-Jácome, J. Escobar, C. Angeles Chávez, E. López Salinas, E. Romero, G. Ferrat, J.A. Toledo-Antonio, *Catal. Today* 130 (2008) 56–62.
- [26] XPS and Auger Handbook, Doc. Number 600001, ThermoVG Scientific: West Sussex U.K., 2 (2003).
- [27] J. Ramirez, L. Ruiz-Ramirez, L. Cedeño, V. Harle, M. Vrinat, M. Breyse, *Appl. Catal. A* 93 (1993) 163–180.
- [28] A. Kukovec, M. Hodos, Z. Konya, I. Kiricsi, *Chem. Phys. Lett.* 411 (2005) 445–449.
- [29] Y.V. Kolen'ko, K.A. Kovnir, A.I. Gavrillov, A.V. Garshev, J. Frantti, O.I. Lebedev, B.R. Churagulov, G.V. Tendeloo, M. Yoshimura, *J. Phys. Chem. B* 110 (2006) 4030–4038.
- [30] R.A. Nyquist, C.L. Putziq, V. Leugers, *Handbook of Infrared and Raman Spectra of Inorganic Compounds and Inorganic Salts*, 1, Academic Press, San Diego, USA, 1997, p. 18.
- [31] E. Payen, M.C. Dhamelincourt, P. Dhamelincourt, J. Grimblot, J.P. Bonnelle, *Appl. Spectrosc.* 36 (1) (1982) 30.
- [32] Z.B. Wei, W. Yan, H. Zhang, T. Ren, Q. Xin, L. Li Zhongcheng, *Appl. Catal. A* 167 (1998) 39–48.
- [33] P.A. Spevack, N.S. McIntyre, *J. Phys. Chem.* 96 (1992) 9029–9035.
- [34] G. Mestl, P. Ruiz, B.H. Delmon Knozinger, *J. Phys. Chem.* 98 (1994) 11269–11275.
- [35] M.A. Cortés-Jacome, G. Ferrat-Torres, L.F. Flores Ortiz, C. Angeles-Chavez, E. Lopez-Salinas, J. Escobar, M.L. Mosqueira, J.A. Toledo-Antonio, *Catal. Today* 126 (2007) 248–255.
- [36] Y. Sakashita, Y. Araki, K. Honna, H. Shimada, *Appl. Catal. A* 197 (2000) 247–253.
- [37] J.R. Günter, O. Marks, T.I. Korányi, Z. Paál, *Appl. Catal.* 39 (1988) 285–294.
- [38] A.I. Dugulan, E.J.M. Hensen, J.A.R. van Veen, *Catal. Today* 130 (2008) 126–134.
- [39] M. Brorson, A. Carlsson, H. Topsøe, *Catal. Today* 123 (2007) 31–36.
- [40] A. Carlsson, M. Brorson, H. Topsøe, *J. Catal.* 227 (2004) 530–536.
- [41] J.C. Muijsers, Th. Weber, V. van Hardeveld, H.W. Zandbergen, J.W. Niemantsverdriet, *J. Catal.* 157 (1995) 698–705.
- [42] Th. Weber, J.C. Muijsers, J.H.M.C. van Wolput, C.P.J. Verhagen, J.W. Niemantsverdriet, *J. Phys. Chem.* 100 (1996) 14144–14150.
- [43] A.F.H. Sanders, A.M. de Jong, V.H.J. de Beer, J.A.R. van Veen, J.W. Niemantsverdriet, *Appl. Surf. Sci.* 144–145 (1999) 380–384.
- [44] J.E. Herrera, D.E. Resasco, *J. Catal.* 221 (2004) 354–364.
- [45] A.D. Gandubert, C. Legens, D. Guillaume, S. Rebours, E. Payen, *Oil Gas Sci. Technol.* 62 (2007) 79–89.
- [46] R. Candia, O. Sorensen, J. Villadsen, N. Topsøe, B.S. Clausen, H. Topsøe, *Bull. Soc. Chim. Belg.* 93 (1984) 763–773.
- [47] Y. Okamoto, T. Kubota, *Catal. Today* 86 (2003) 31–43.
- [48] H. Topsøe, B.S. Clausen, N. Topsøe, P. Zeuthen, *Stud. Surf. Sci. Catal.* 53 (1989) 77–102.
- [49] A.M. De Jong, H.J. Borg, L.J. Van Ijzendoorn, V.G.F.M. Soudant, V.H.J. De Beer, J.A.R. Van Veen, J.W. Niemantsverdriet, *J. Phys. Chem.* 97 (1993) 6477–6483.
- [50] H. Topsøe, *Appl. Catal. A* 322 (2007) 3–8.